The fire resistance of high-strength concrete containing natural zeolites

Alexandra R. L. Kushnir[1], Michael J. Heap[1]*, Luke Griffiths[1,2], Fabian B. Wadsworth[3], Alessio Langella[4], Patrick Baud[1], Thierry Reuschlé[1], Jackie E. Kendrick[5], James E. P. Utley[5]

[1]*Université de Strasbourg, CNRS, ENGEES, Institut Terre et Environnement de Strasbourg, UMR 7063, 5 rue René Descartes, Strasbourg F-67084, France*

[2]*NGI – Norwegian Geotechnical Institute, Oslo, 0806, Norway*

[3]*Department of Earth Sciences, Science Labs, Durham University, Durham, DH1 3LE, U.K.*

[4]*Department of Science and Technology, University of Sannio, Via De Sanctis snc, 82100 Benevento, Italy*

[5]*Department of Earth and Ocean Sciences, University of Liverpool, Liverpool L69 3BX, U.K.*

*Corresponding author: Michael Heap (heap@unistra.fr)

Key words: concrete; tuff; zeolite; climate change; fire; uniaxial compressive strength

Abstract

More sustainable and environmentally friendly concretes are essential to reduce the climatic and environmental impact of the growing demand for concrete to fuel urban sprawl. This manuscript reports on an experimental study designed to test the fire resistance of one such concrete, prepared to contain natural zeolite-bearing tuff. The fire resistance of concretes containing natural zeolites has received little attention and is therefore poorly understood. Relative reductions in residual uniaxial compressive strength as a function of increasing temperature (up to 1000 °C) were very similar for the reference concrete (containing no tuff) and the tuff-bearing concrete. These data can be explained by the similar influence of high-temperature on the chemical (dehydroxylation reactions) and physical (microcracking and porosity) properties of both concretes. The satisfactory performance of the concrete containing natural zeolites following fire is welcome owing to the economic, climatic, and environmental benefits of using natural pozzolan and aggregate substitutes.

1 Introduction

In the last decades, the consumption of cement concretes has grown enormously and the cement and concrete industry are significant contributors to the increase in atmospheric CO_2 fuelling the current climate crisis (e.g., [1]). Indeed, the cement and concrete industry are responsible for about 5-7% of global anthropogenic CO_2 emissions (e.g., [1-2]). The majority of these emissions are a result of CO_2 liberation as limestone is converted to lime in the manufacture of cement (e.g., [1]). The extraction of sand to meet the demand for concrete puts further strain on the environment [3]. As a result, replacing or partially replacing traditional ingredients, such as Portland cement and quartz sand aggregates, with alternative materials is viewed as a viable method to reduce the environmental impact of cement and concrete production (e.g., [2]).

Natural pozzolanic materials such as natural zeolites, which can be sourced from quarrying and industrial waste, are considered as a suitable replacement material for Portland cement and/or aggregates in the production of concrete (e.g., [4]). The use of zeolitic tuff, a volcanic rock rich in natural zeolites, in concrete manufacture can be traced back thousands of years (e.g., [5]). Indeed, Roman architect Vitruvius commented on the durability of concretes prepared using zeolitic tuff in his famous *De Architectura* works in the late first century BCE. Two thousand years later, structures built by the Romans using tuff-bearing concrete can still be found largely intact, a testament to their high strength, durability, and resistance to weathering (e.g., [6-9]). More recently, considerable effort has been spent investigating the effectiveness of using natural zeolite as a supplementary cementitious material and/or aggregate, most of which show that the addition of natural zeolites leads to an improvement of the mechanical strength, durability properties, and/or weather resistance of cement and concrete (e.g., [2,10-26]). In cases in which improvements to concrete performance were not observed, or performance was diminished, it was concluded that natural zeolites still offer an economically and environmentally friendly pozzolan substitute (e.g., [27]).

Exposure to high temperature as a result of the exposure to, for example, fire, lava, or nuclear meltdown, is well known to negatively impact the physical and mechanical properties of concrete (e.g., [28-29] and references therein). For example, uniaxial compressive strength of high-strength concrete decreases as a function of increasing thermal stressing temperature (e.g., [29-49]). In their review of the available data, Heap et al. [29] found that the relative residual uniaxial compressive strength of concrete is reduced to < 0.4 following exposure to 1000 °C, and that the aggregate type plays a secondary role to the cement in determining the fire resistance of high-strength concretes.

Despite the wealth of studies focussed on assessing the influence of temperature on the physical and mechanical properties of high-strength concretes, few assess the fire resistance of

concretes containing natural zeolites. Karakurt and Topçu [50], for example, found that the compressive strength of zeolite-bearing concrete was reduced at temperatures above 100 °C, whereas the strength reduction in the other concretes tested, using a range of blended cements, occurred at temperatures > 450 °C. Akçaözoğlu et al. [51] found that replacing Portland cement with increasing amounts of clinoptilolite did not influence the strength reduction following exposure to high temperature (up to 750 °C). Alternatively, Beycioglu et al. [52] found that strength reductions in cements containing 15-20% clinoptilolite were higher than those for cements containing 0-10% clinoptilolite following exposure to temperatures up to 500 °C. Motivated by the paucity of studies on the high-temperature resistance of natural zeolite-bearing concretes, this manuscript presents a laboratory study that provides residual uniaxial compressive strength data for concrete prepared with and without natural zeolites following exposure to high temperature (up to 1000 °C). Ancillary experiments (porosity measurements, acoustic emission monitoring during heating and cooling, and thermo-gravimetric analysis) and microstructural and mineral content analyses (backscattered scanning electron microscopy and QEMSCAN^{TM} analysis) were used to assist in the interpretation of the mechanical data. Assessing the performance of economically and environmentally friendly concretes, such as their fire resistance, is important to the promotion of their use in light of the climatic and environmental impact of the rapidly growing cement and concrete industry.

2 Materials and methods

To investigate the influence of tuff powder on the thermal resistance of concrete, two concretes were prepared. These concretes were prepared such that their ingredients were identical with the exception that one concrete contains tuff powder while the other contains an aggregate of similar grain size. Table 1 shows the ingredients, and their proportions, for both concretes. If the tuff powder is considered as a binder, the water/binder ratio of the reference

and tuff-bearing concretes are 0.69 and 0.53, respectively. Although these mixes yield concretes with different strengths (see the Results section), and comparable strengths could have been achieved by, for example, changing the aggregate type [53], it was considered important to only vary one ingredient in the present study, which aims to assess the fire resistance of concrete containing natural tuff powder. The concrete containing the tuff powder will hereafter be referred to as "tuff-bearing concrete", and the concrete without the tuff powder as "reference concrete". The tuff used was a powder of a yellow-coloured zeolitised tuff from the Campanian Ignimbrite, collected from a quarry in Comiziano in Italy (the same tuff used in de Gennaro et al. [54]). The mineral composition of the tuff is given in Table 2 [54]. The gravel and sand used for both concretes (Table 1) was predominately dolomite. Backscattered scanning electron microscope images of both concretes are shown in Figure 1. These images show that there is porosity at the aggregate boundaries in the tuff-bearing concrete that is not present in the reference concrete (Figure 1). The cement matrix of the tuff-bearing concrete also appears more porous than that of the reference concrete (Figure 1).

Cylindrical samples were cored from the blocks of concrete, all of the same age and aged to >> 28 days, to a diameter of 25 mm. The ends of the samples were ground flat and parallel to a nominal sample length of 50 mm. This diameter was chosen so that the physical and mechanical properties, such as porosity and uniaxial compressive strength, could be measured on the same cylindrical samples. Prior to all measurements, all samples were cleaned with water and dried in a vacuum oven at 40 °C for a minimum of 48 hours (to remove any water from inside the void space within the samples). The cylindrical samples of both concretes were either kept intact (hereafter referred to as "as-prepared"), or thermally stressed in a box furnace to temperatures of 100, 200, 300, 500, 750, or 1000 °C. The thermally stressed samples were heated to and cooled from their target temperature at a rate of 1 °C/min. The samples were left at their target temperature for two hours before cooling to ensure thermal equilibrium at the

target temperature. The time constant for temperature equilibrium can be estimated using r^2/d, where r is the sample radius and d is the thermal diffusivity of the sample. Taking $r = 1.25 \times 10^{-2}$ m^2 and $d = 9.0 \times 10^{-7}$ m^2/s (see the Results section), the time constant for temperature equilibrium is estimated to be 174 s, ensuring that our samples are at or close to thermal equilibrium during heating/cooling.

2.1 Thermal conductivity

The thermal conductivity and thermal diffusivity of as-prepared samples of both concretes were measured using the transient plane heat source method using a Hot Disk TPS 500 Thermal Constants Analyser [55-56]. A 6.4 mm-radius Kapton-insulated sensor was placed between a 25 mm-diameter cylindrical sample of each concrete type and a piece of polyurethane foam of known thermal properties. The output power used was 200 mW and the measurement duration was 20 s. Four consecutive measurements were performed on each sample and an average of these four measurements is reported herein. Prior to each measurement, the thermal equilibrium of each sample was ensured. More details on this method of thermal property determination can be found in Harlé et al. [57] and Heap et al. [58].

2.2 Gas permeability

Permeability was measured on a cylindrical sample of each of the as-prepared concretes in a benchtop nitrogen-gas permeameter (detailed schematics of the device are provided in [59-60]). The confining pressure used for both experiments was 1 MPa. Both samples were left to equilibrate at the confining pressure for one hour, after which the permeability was measured using the pulse-decay technique [61]. To do so, the pore pressure differential was set at 0.2 MPa, the valve between the nitrogen gas bottle and sample was closed, and the decay in pressure as a function of time was monitored. The data were also checked for the Forchheimer [62] and

Klinkenburg [63] corrections. The data collected for this study required a Klinkenberg correction. More details on this method of permeability determination can be found in Heap et al. [64]. Permeability measurements were conducted at ambient laboratory temperature.

2.3 Thermo-gravimetric analysis

To determine the dominant temperature-induced mineralogical changes in both concretes with increasing temperature, thermo-gravimetric analysis (TGA) were performed on powdered samples (55 to 60 mg) of each concrete using a Netzsch Pegasus 404 simultaneous thermal analysis device. Powders were heated in an argon-flushed atmosphere inside a platinum crucible (with lid). All powders were initially heated to 100 °C for 20 min to ensure that any free water (i.e. non-structurally bound) was first removed. Powders were then subjected to two heating-cooling cycles during which they were heated to 1050 °C at a rate of 25 °C/min and cooled to room temperature at the same rate. It is noted here that the heating/cooling rates used in the TGA experiments, 25 °C/min, are higher than those used when thermally-stressing the samples, see above, and those used in the acoustic emission monitoring experiments described in the next subsection. However, the thermal-stressing and acoustic emission monitoring experiments were performed on 25 mm-diameter samples, whereas the TGA experiments were performed on powdered samples. Importantly, the powdered samples used in the TGA experiments were in thermal equilibrium at the imposed heating/cooling rate. This analysis was used to track the mass loss in each sample as a result of temperature-induced mineral reactions (e.g., dehydroxylation reactions).

2.4 Acoustic emission monitoring during heating

To determine the onset of thermally induced microcracking in both samples, acoustic emissions (AE), a proxy for the initiation and growth of microcracks (e.g., [65]), were

monitored during heating and cooling for both concretes. A 25 mm-diameter sample was placed between two steel pistons, one of which contained a wideband (100-1000 Hz) AE sensor (from Physical Acoustics) that was connected to a USB AE Node (from MISTRAS Group: a single channel AE digital signal processor with a built-in 26 dB pre-amplifier). The pistons and sample were mounted into a LoadTrac II uniaxial press. A low axial force of 491 N (equating to an axial stress of 1 MPa on a 25 mm-diameter sample) was applied to the sample to ensure sufficient coupling between the sample and the pistons. The applied force was kept constant during heating and cooling using the servo-controlled stepper motor of the LoadTrac II. A tube-furnace, positioned such that the sample was at its centre, heated the sample to 700 °C at a rate of 1 °C/min. The furnace temperature was held at 700 °C for two hours before cooling back to room temperature at a maximum rate of 1 °C/min. A maximum temperature of 700 °C was chosen to avoid damaging the AE sensor. A detailed description of this apparatus can be found in Griffiths et al. [66].

2.5 Porosity and density measurements

Prior to any thermal stressing, the initial connected porosity of all the prepared 25 mm-diameter samples was calculated using the skeletal volume provided by a Micrometrics AccuPycII 1340 helium pycnometer and the bulk sample volume determined using the sample dimensions. The connected porosity of the samples was remeasured following thermal stressing. Measurements of porosity were conducted at ambient laboratory temperature. The dry bulk sample density of each sample was calculated before and after heating using the sample mass, measured using a precision (three decimal places) balance, and the bulk sample volume.

2.6 Uniaxial compressive strength (UCS)

Finally, the as-prepared and thermally stressed samples were deformed uniaxially in a servo-controlled uniaxial press under ambient laboratory conditions at a constant strain rate of 10^{-5} s^{-1} until macroscopic failure. Axial load and displacement were continuously recorded during deformation by a load cell and a linear variable differential transducer, respectively. The deformation of the loading chain was subtracted from the displacement. These values were converted to axial stress and axial strain using the sample dimensions. A lubricating wax was applied to both ends of each sample before deformation to minimise end effects associated with friction and shear stress build-up at the sample-piston interface.

2.7 Microstructural analysis

To understand the microstructural changes as a consequence of thermal stressing, thin sections were prepared of samples of each concrete that had been thermally stressed to a temperature of 750 °C. Their microstructure was examined using a Tescan Vega 2 XMU system backscattered SEM.

2.8 Quantitative element mapping

The prepared thin sections (as-prepared and thermal stressed samples of both concretes) were also analysed using QEMSCAN™ (Quantitative Evaluation of Minerals by SCANing electron microscopy), an automated SEM-EDS system for mapping mineral distribution and quantitative mineral modality. The QEMSCAN™ WellSite at the University of Liverpool uses a 15 kV accelerating voltage and ~5 nA beam current. Secondary X-rays emitted by the sample are recorded by two Bruker energy dispersive X-ray spectrometers and processed to identify and quantify the elements present and output a chemical composition. The chemical composition is compared to an extensive mineral database (e.g., [67-68]). Based on prior knowledge of the componentry of the concrete samples (Tables 1 and 2), a user modified

version of the database was used. The system does not measure crystallographic features, thus cannot differentiate between chemically identical polymorphs or amorphous or crystalline phases. Data was collected in field-scan mode collecting X-rays (here, 1500 X-rays per point) in an automated raster pattern (e.g., [67]), with X-rays collected at 20 μm intervals over the whole thin section for bulk mineralogy, and at 2 μm step size over six 1.5 mm square areas (each area separated by 5 mm, to give a representative collage) to examine the cement matrix textures. There is no influence of step size on the measured mineralogy as there is no change in the beam operating conditions, only the spacing between analyses. Data processing was performed using the iDiscover software, which stitches the acquired data into coloured maps where each colour represents a different phase. The grouping of minerals/phases, and the colours used to represent them, is user controlled. The sum of pixels of each phase are normalised to provide quantitative modal mineralogy on a pore-free basis (e.g., [69-71]). Wallace et al. [71] give maximum standard deviations of < 0.39% for all phases based on repeat scans after removing and reinserting the same thin section. Phases (minerals, glasses, and amorphous phases) defined in the SIP list include subcategories for pure and impure varieties, and mixtures of the phase with some other common phases. These subcategories successfully deal with most occasions the beam interacts with multiple phases at one point. Single pixels that have not been successfully classified by the aforementioned procedures but are surrounded entirely by pixels of one phase have been added to the tally of the surrounding phase at the users discretion.

3 Results

The average thermal conductivity and thermal diffusivity of both concretes was found to be similar. The average thermal conductivity of the as-prepared reference and tuff-bearing concretes was measured to be 2.338 ± 0.100 and 2.126 ± 0.0083 W/mK, respectively. Their

average thermal diffusivities are 0.902 ± 0.084 and 0.918 ± 0.087 mm^2/s, respectively. The gas permeabilities of as-prepared reference and tuff-bearing concretes were measured to be 2.17×10^{-17} and 1.63×10^{-16} m^2, respectively.

The relative mass loss as a function of temperature is similar for both concretes (Figure 2). Large decreases in sample mass are observed at temperatures ≥ 750 °C (Figure 2). The mass of the samples did not decrease further as temperature was increased above 920 °C (Figure 2). At the end of the experiments, the relative masses of the reference and tuff-bearing concretes were 0.57 and 0.54, respectively (Figure 2).

The cumulative number of AE hits during heating and cooling as a function of temperature for the two concretes are shown in Figure 3. For both concretes, the first AE hits were recorded at a temperature of ~100-200 °C and, at a temperature of about 400-450 °C, the rate of AE activity increased substantially (Figure 3). The cumulative number of AE hits increased as temperature increased from 400-450 °C to the maximum temperature of 700 °C (Figure 3). More AE hits were recorded during the cooling of both concretes than during the heating (Figure 3).

The average initial connected porosity and bulk sample density of the reference and tuff-bearing concretes was measured to be 0.085 and 0.108 and 2529 and 2475 kg/m^3, respectively (data are given in Table 3). Connected porosity and relative change in connected porosity as a function of thermal stressing temperature are shown in Figures 4a and 4b, respectively. For both concretes, increases to connected porosity are small up to 500 °C, and large at 750 and 1000 °C (Figure 4). For example, connected porosity increased to ~0.57 for both concretes following exposure to a temperature of 1000 °C (Figure 4a). The relative change in connected porosity at 750 and 1000 °C is slightly higher for the reference concrete than for the tuff-bearing concrete (Figure 4b).

Representative uniaxial stress-strain curves for the reference and tuff-bearing concretes exposed to different thermal stressing temperatures are shown in Figures 5a and 5b, respectively. All the samples failed by axial splitting. The UCS and relative uniaxial compressive strength (as a fraction) are shown as a function of thermal stressing temperature in Figures 6a and 6b, respectively, and UCS is shown as a function of connected porosity in Figure 6c (strength data are given in Table 3). The UCS of the as-prepared reference concrete is higher (~91 MPa) than the as-prepared tuff-bearing concrete (~58 MPa) (Figures 5 and 6). The UCS of both concretes is reduced as thermal stressing temperature increases (Figures 5 and 6). The UCS of the reference concrete remains higher than that of the tuff-bearing concrete at all thermal stressing temperatures except 1000 °C (values of UCS at 1000 °C are essentially equal). The relative decrease in UCS as a function of temperature is approximately constant for the two concretes (Figure 6b). Figure 6c shows that the UCS of the two concretes decreases as a function of increasing connected porosity.

Backscattered SEM images of both concretes following exposure to 750 °C are shown in Figures 7 and 8. Figure 7 shows that, at 750 °C, both concretes contain microcracks that preferentially grow at the boundary between the aggregates, but that they also pass through the cement paste (matrix). Figure 8 shows that the aggregates are microcracked and contain sub-circular pores (diameter = 5-10 μm) that are not observed in the as-prepared concretes (Figure 1). QEMSCAN^{TM} mineral composition maps for the as-prepared reference concrete and tuff-bearing concrete, and samples of both concretes heated to and cooled from 750 °C, are shown in Figures 9 and 10, respectively. Figure 11 provides pie charts showing the mineral composition of both concretes before and after exposure to 750 °C (data provided in Table 4). As expected, the as-prepared concretes are predominantly dolomite, and the tuff-bearing concrete contains a richer assortment of minerals (Figures 11a and 11c; Table 4). The most obvious change to both samples following exposure to 750 °C is the decarbonation of dolomite

to form magnesium and calcium oxides (Figures 11b and 11d), which occurs at the outermost edge of the dolomite aggregate clasts (Figures 9c and 10c and 10d). Other notable changes in both concretes include the reduction in tetracalcium aluminoferrite and gypsum/anhydrite (Figure 11; Table 4). Illite content in the tuff-bearing concrete, not present in the reference concrete, was also reduced following exposure to 750 °C (Figure 11; Table 4).

4 Discussion

The mechanical property data show that the as-prepared reference concrete has a higher uniaxial compressive strength than the as-prepared tuff-bearing concrete (Figures 5 and 6; Table 3). Because porosity plays a first-order role in governing the compressive strength of cements and concretes (e.g., [72-74]), the higher porosity of the tuff-bearing concrete (the average initial connected porosity of the reference and tuff-bearing concretes was 0.085 and 0.108, respectively; Table 3) can explain its lower strength. Microstructural observations show that the tuff-bearing concrete contains porosity at the boundaries of the aggregates (Figure 1). An increase in porosity as a function of zeolite content in cements and concretes has been reported in previous studies, and is a consequence of pozzolanic reactions involving high-surface area zeolites (e.g., [17,23,26-27]). The higher porosity of the tuff-bearing concrete could also be a result of the lower water/binder ratio (Table 1). This increase in porosity, however, also reduces the thermal conductivity (the thermal conductivity of the as-prepared reference and tuff-bearing concretes was 2.338 ± 0.100 and 2.126 ± 0.0083 W/mK, respectively) of the concrete. The tuff-bearing concrete measured herein will therefore serve as a better thermal insulator than the reference concrete (see also [17,23]). However, the higher permeability (the permeability of the as-prepared reference and tuff-bearing concretes was 2.17×10^{-17} and 1.63×10^{-16} m^2, respectively) and porosity of the tuff-bearing concrete could lead to problems related to the ingress of liquids (e.g., [75-76]).

The observed decrease in residual strength as a function of increasing temperature (Figure 6a) is in general agreement with the wealth of previously published data on high-strength concretes (see Heap et al. [29] and references therein). Importantly, the results also show that the relative decrease in residual strength is very similar for both concretes (Figure 6b). The similarity in relative strength reduction (Figure 6b) can be explained by the similar relative increase in connected porosity (Figure 4b) because, as discussed above, porosity plays a first-order role in dictating the strength of cements and concretes (e.g., [72-74]). Indeed, Figure 6c shows that UCS decreases as a function of increasing connected porosity. The increase in connected porosity in both concretes is principally the result of two mechanisms: dehydroxylation reactions and thermal microcracking.

Dehydroxylation reactions are monitored by thermogravimetric (Figure 2) and QEMSCAN^{TM} analyses (Figures 9-11; Table 4). The thermogravimetric analysis (Figure 2) shows that substantial mass reductions in both concretes were observed at temperatures > 750 °C (Figure 2). Mass loss at this temperature is the result of the two-stage decarbonation of dolomite (e.g., [77-79]), a process that first affects the outermost edge of the dolomite aggregate clasts (Figures 9c and 10c and 10d). A result of decarbonation is that the aggregates, now composed or partially composed of magnesium and calcium oxides (Figures 9-11; Table 4), contain many intragranular microcracks and pores (Figure 8). Importantly, the mass loss as a function of temperature is essentially the same for the reference and tuff-bearing concrete (Figure 2). Indeed, previous studies have also shown that the relative mass change of concrete as a function of temperature did not change as zeolite content increased [80]. Although the temperature estimated for decarbonation will depend on the heating rate used in the thermogravimetric tests [81], it can be confidently stated using these data (obtained a rate of 25 °C/min) that the large changes in the physical and mechanical properties of the concretes heated to 750 and 1000 °C are due to the decarbonation of the dolomite aggregates.

Thermal microcracking, monitored by the output of AE activity, was observed to start at ~100-200 °C and increased significantly at a temperature of 400-450 °C in both concretes (Figure 3). The measured onset temperature for thermal microcracking (~100-200 °C) is in agreement with that found for siliceous-aggregate, high-strength concrete (180 °C; [29]). Ozawa et al. [82] also found that only a very small number of AE hits were recorded as high-strength concrete was heated from 50 to 100 °C, but that substantially more AE hits were recorded from 100 to 200 °C. Thermal microcracking in these concretes is the result of the thermal expansion mismatch of different minerals and the dehydroxylation of the cement and aggregates, both of which generate stresses that result in microcracking (e.g., Heap et al. [29]). Microstructural observations corroborate these data, showing that exposure to high temperature results in the formation of microcracks in both concretes (Figure 7).

It follows that, because the mass loss as a function of temperature (Figure 2) and the onset of thermal microcracking (Figure 3) are very similar for both concretes, the relative increase in porosity (Figure 4b) and therefore the relative reduction in residual strength following exposure to high temperature are also similar (Figure 6b).

5 Conclusions

Motivated by the need for more sustainable and environmentally friendly alternatives for traditional concretes, this manuscript presents an experimental study designed to test the fire resistance of a concrete prepared to contain natural zeolite-bearing tuff. The data show that relative reductions in strength as a function of increasing temperature (up to 1000 °C) were very similar for the reference concrete (containing no tuff) and the tuff-bearing concrete. These data can be explained by (1) their similar relative increase in porosity and (2) their similar response to high-temperature in terms of their chemical (dehydroxylation reactions) and physical (microcracking) properties.

To conclude, although the physical and mechanical properties of zeolite-bearing tuffs are negatively influenced by exposure to high-temperature (e.g., [83-84]), the fire resistance of the prepared tuff-bearing concrete is similar to that of the reference concrete (that contains no tuff). This conclusion is welcome due to the climatic and environmental benefit of using natural pozzolan and aggregate substitutes. Based on these data, no special considerations would be required regarding the fire resistance of buildings constructed using tuff-bearing concrete. However, more research should now be conducted to better understand the fire resistance of concretes prepared to contain different natural zeolites and different proportions of natural zeolite.

References

[1] Mahasenan, N., Smith, S., & Humphreys, K. (2003). The cement industry and global climatechange: current and potential future cement industry CO_2 emissions. In *Greenhouse Gas Control Technologies-6th International Conference* (pp. 995-1000). Pergamon.

[2] Najimi, M., Sobhani, J., Ahmadi, B., & Shekarchi, M. (2012). An experimental study on durability properties of concrete containing zeolite as a highly reactive natural pozzolan. *Construction and Building Materials, 35*, 1023-1033.

[3] Torres, A., Brandt, J., Lear, K., & Liu, J. (2017). A looming tragedy of the sand commons. *Science, 357*(6355), 970-971.

[4] Ahmadi, B., & Shekarchi, M. (2010). Use of natural zeolite as a supplementary cementitious material. *Cement and Concrete Composites, 32*(2), 134-141.

[5] Colella, C., Gennaro, M. D., & Aiello, R. (2001). Use of zeolitic tuff in the building industry. *Reviews in Mineralogy and Geochemistry*, *45*(1), 551-587.

[6] Jackson, M. D., Moon, J., Gotti, E., Taylor, R., Chae, S. R., Kunz, M., ... & Wenk, H. R. (2013). Material and elastic properties of Al-tobermorite in ancient Roman seawater concrete. *Journal of the American Ceramic Society*, *96*(8), 2598-2606.

[7] Jackson, M. D., Chae, S. R., Mulcahy, S. R., Meral, C., Taylor, R., Li, P., ... & Wenk, H. R. (2013). Unlocking the secrets of Al-tobermorite in Roman seawater concrete. *American Mineralogist*, *98*(10), 1669-1687.

[8] Jackson, M. D., Landis, E. N., Brune, P. F., Vitti, M., Chen, H., Li, Q., ... & Ingraffea, A. R. (2014). Mechanical resilience and cementitious processes in Imperial Roman architectural mortar. *Proceedings of the National Academy of Sciences*, *111*(52), 18484-18489

[9] Brandon, C. J., Hohlfelder, R. L., Jackson, M. D., & Oleson, J. P. (2014). *Building for eternity: the history and technology of Roman concrete engineering in the sea*. Oxbow Books.

[10] Chan, S. Y., & Ji, X. (1999). Comparative study of the initial surface absorption and chloride diffusion of high performance zeolite, silica fume and PFA concretes. *Cement and Concrete Composites*, *21*(4), 293-300.

[11] Poon, C. S., Lam, L., Kou, S. C., & Lin, Z. S. (1999). A study on the hydration rate of natural zeolite blended cement pastes. *Construction and Building Materials*, *13*(8), 427-432.

[12] Canpolat, F., Yılmaz, K., Köse, M. M., Sümer, M., & Yurdusev, M. A. (2004). Use of zeolite, coal bottom ash and fly ash as replacement materials in cement production. *Cement and Concrete Research*, *34*(5), 731-735.

[13] de Gennaro, R., Cappelletti, P., Cerri, G., de Gennaro, M., Dondi, M., & Langella, A. (2005). Neapolitan Yellow Tuff as raw material for lightweight aggregates in lightweight structural concrete production. *Applied Clay Science*, *28*(1-4), 309-319.

[14] de Gennaro, R., Cappelletti, P., Cerri, G., De'Gennaro, M., Dondi, M., Graziano, S. F., & Langella, A. (2007). Campanian Ignimbrite as raw material for lightweight aggregates. *Applied Clay Science*, *37*(1-2), 115-126.

[15] Albayrak, M., Yörükoğlu, A., Karahan, S., Atlıhan, S., Aruntaş, H. Y., & Girgin, İ. (2007). Influence of zeolite additive on properties of autoclaved aerated concrete. *Building and Environment*, *42*(9), 3161-3165.

[16] Ikotun, B. D., & Ekolu, S. (2010). Strength and durability effect of modified zeolite additive on concrete properties. *Construction and Building Materials*, *24*(5), 749-757.

[17] Karakurt, C., Kurama, H., & Topcu, I. B. (2010). Utilization of natural zeolite in aerated concrete production. *Cement and Concrete Composites*, *32*(1), 1-8.

[18] Shekarchi, M., Ahmadi, B., & Najimi, M. (2012). Use of natural zeolite as pozzolanic material in cement and concrete composites. In: Handbook of Natural Zeolites (Eds: Inglezakis, V.J. and Zopas, A.A.). DOI: 10.2174/97816080526151120101.

[19] Ramezanianpour, A. A., Kazemian, A., Sarvari, M., & Ahmadi, B. (2012). Use of natural zeolite to produce self-consolidating concrete with low Portland cement content and high durability. *Journal of Materials in Civil Engineering*, *25*(5), 589-596.

[20] Sabet, F. A., Libre, N. A., & Shekarchi, M. (2013). Mechanical and durability properties of self consolidating high performance concrete incorporating natural zeolite, silica fume and fly ash. *Construction and Building Materials*, *44*, 175-184.

[21] Ahmadi, B., Sobhani, J., Shekarchi, M., & Najimi, M. (2014). Transport properties of ternary concrete mixtures containing natural zeolite with silica fume or fly ash. *Magazine of Concrete Research*, *66*(3), 150-158.

[22] Valipour, M., Yekkalar, M., Shekarchi, M., & Panahi, S. (2014). Environmental assessment of green concrete containing natural zeolite on the global warming index in marine environments. *Journal of Cleaner Production*, *65*, 418-423.

[23] Vejmelková, E., Koňáková, D., Kulovaná, T., Keppert, M., Žumár, J., Rovnaníková, P., ... & Černý, R. (2015). Engineering properties of concrete containing natural zeolite as supplementary cementitious material: Strength, toughness, durability, and hygrothermal performance. *Cement and Concrete Composites*, *55*, 259-267.

[24] Markiv, T., Sobol, K., Franus, M., & Franus, W. (2016). Mechanical and durability properties of concretes incorporating natural zeolite. *Archives of Civil and Mechanical Engineering*, *16*(4), 554-562.

[25] Mohseni, E., Tang, W., & Cui, H. (2017). Chloride diffusion and acid resistance of concrete containing zeolite and tuff as partial replacements of cement and sand. *Materials*, *10*(4), 372.

[26] Girskas, G., & Skripkiūnas, G. (2017). The effect of synthetic zeolite on hardened cement paste microstructure and freeze-thaw durability of concrete. *Construction and Building Materials*, *142*, 117-127.

[27] Valipour, M., Pargar, F., Shekarchi, M., & Khani, S. (2013). Comparing a natural pozzolan, zeolite, to metakaolin and silica fume in terms of their effect on the durability characteristics of concrete: A laboratory study. *Construction and Building Materials*, *41*, 879-888.

[28] Phan, L. T., & Carino, N. J. (1998). Review of mechanical properties of HSC at elevated temperature. *Journal of Materials in Civil Engineering*, *10*(1), 58-65.

[29] Heap, M. J., Lavallée, Y., Laumann, A., Hess, K. U., Meredith, P. G., Dingwell, D. B., ... & Weise, F. (2013). The influence of thermal-stressing (up to 1000 C) on the physical, mechanical, and chemical properties of siliceous-aggregate, high-strength concrete. *Construction and Building Materials*, *42*, 248-265.

[30] Chan, S. Y., Peng, G. F., & Chan, J. K. (1996). Comparison between high strength concrete and normal strength concrete subjected to high temperature. *Materials and Structures*, *29*(10), 616.

[31] Chan, Y. N., Peng, G. F., & Anson, M. (1999). Residual strength and pore structure of high-strength concrete and normal strength concrete after exposure to high temperatures. *Cement and concrete composites*, *21*(1), 23-27.

[32] Chan, Y. N., Luo, X., & Sun, W. (2000). Compressive strength and pore structure of high-performance concrete after exposure to high temperature up to 800 C. *Cement and Concrete Research*, *30*(2), 247-251.

[33] Luo, X., Sun, W., & Chan, S. Y. N. (2000). Effect of heating and cooling regimes on residual strength and microstructure of normal strength and high-performance concrete. *Cement and Concrete Research*, *30*(3), 379-383.

[34] Hoff, G. C., Bilodeau, A., & Malhotra, V. M. (2000). Elevated temperature effects on HSC residual strength. *Concrete International*, *22*(4), 41-48.

[35] Phan, L. T., Lawson, J. R., & Davis, F. L. (2001). Effects of elevated temperature exposure on heating characteristics, spalling, and residual properties of high performance concrete. *Materials and structures*, *34*(2), 83-91.

[36] Poon, C. S., Azhar, S., Anson, M., & Wong, Y. L. (2001). Comparison of the strength and durability performance of normal-and high-strength pozzolanic concretes at elevated temperatures. *Cement and Concrete Research*, *31*(9), 1291-1300.

[37] Poon, C. S., Azhar, S., Anson, M., & Wong, Y. L. (2001). Strength and durability recovery of fire-damaged concrete after post-fire-curing. *Cement and Concrete Research*, *31*(9), 1307-1318.

[38] Phan, L. T., & Carino, N. J. (2002). Effects of test conditions and mixture proportions on behavior of high-strength concrete exposed to high temperatures. *ACI Materials Journal*, *99*(1), 54-66.

[39] Li, M., Qian, C., & Sun, W. (2004). Mechanical properties of high-strength concrete after fire. *Cement and Concrete Research*, *34*(6), 1001-1005.

[40] Chen, B., & Liu, J. (2004). Residual strength of hybrid-fiber-reinforced high-strength concrete after exposure to high temperatures. *Cement and Concrete Research*, *34*(6), 1065-1069.

[41] Fu, Y. F., Wong, Y. L., Poon, C. S., & Tang, C. A. (2005). Stress–strain behaviour of high-strength concrete at elevated temperatures. *Magazine of Concrete Research*, *57*(9), 535-544.

[42] Husem, M. (2006). The effects of high temperature on compressive and flexural strengths of ordinary and high-performance concrete. *Fire Safety Journal*, *41*(2), 155-163.

[43] Xiao, J., & Falkner, H. (2006). On residual strength of high-performance concrete with and without polypropylene fibres at elevated temperatures. *Fire safety journal*, *41*(2), 115-121.

[44] Yan, X., Li, H., & Wong, Y. L. (2007). Assessment and repair of fire-damaged high-strength concrete: Strength and durability. *Journal of Materials in Civil Engineering*, *19*(6), 462-469.

[45] Raju, M. P., Srinivasa Rao, K., & Raju, P. S. N. (2007). Compressive strength of heated high-strength concrete. *Magazine of Concrete Research*, *59*(2), 79-85.

[46] Behnood, A., & Ghandehari, M. (2009). Comparison of compressive and splitting tensile strength of high-strength concrete with and without polypropylene fibers heated to high temperatures. *Fire Safety Journal*, *44*(8), 1015-1022.

[47] Noumowé, A., Siddique, R., & Ranc, G. (2009). Thermo-mechanical characteristics of concrete at elevated temperatures up to 310 C. *Nuclear Engineering and Design*, *239*(3), 470-476.

[48] Tang, W. C., & Lo, T. Y. (2009). Mechanical and fracture properties of normal-and high-strength concretes with fly ash after exposure to high temperatures. *Magazine of Concrete Research*, *61*(5), 323-330.

[49] Siddique, R., & Noumowé, A. N. (2010). An overview of the properties of high-strength concrete subjected to elevated temperatures. *Indoor and Built Environment*, *19*(6), 612-622.

[50] Karakurt, C., & Topçu, İ. B. (2012). Effect of blended cements with natural zeolite and industrial by-products on rebar corrosion and high temperature resistance of concrete. *Construction and Building Materials*, *35*, 906-911.

[51] Akçaözoğlu, K., Fener, M., Akçaözoğlu, S., & Öcal, R. (2014). Microstructural examination of the effect of elevated temperature on the concrete containing clinoptilolite. *Construction and Building Materials*, *72*, 316-325.

[52] Beycioglu, A., Aruntaş, H. Y., Gencel, O., Lobland, H. E. H., Şamandar, A., & Brostow, W. (2016). Effect of elevated temperatures on properties of blended cements with clinoptilolite. *Materials Science*, *22*(4), 548-552.

[53] Wu, K. R., Chen, B., Yao, W., & Zhang, D. (2001). Effect of coarse aggregate type on mechanical properties of high-performance concrete. *Cement and Concrete Research*, *31*(10), 1421-1425.

[54] de Gennaro, R., Langella, A., D'Amore, M., Dondi, M., Colella, A., Cappelletti, P., & de Gennaro, M. (2008). Use of zeolite-rich rocks and waste materials for the production of structural lightweight concretes. *Applied Clay Science*, *41*(1-2), 61-72.

[55] Gustafsson, S. E. (1991). Transient plane source techniques for thermal conductivity and thermal diffusivity measurements of solid materials. Review of Scientific Instruments, 62(3), 797-804.

[56] Gustavsson, M., Karawacki, E., & Gustafsson, S. E. (1994). Thermal conductivity, thermal diffusivity, and specific heat of thin samples from transient measurements with hot disk sensors. Review of Scientific Instruments, 65(12), 3856-3859.

[57] Harlé, P., Kushnir, A.R.L., Aichholzer, C., Heap, M.J., Hehn, R., Maurer, V., Baud, P., Richard, A., Genter, A., Duringer, Ph. (2019) Heat flow estimates in the Upper Rhine Graben using laboratory measurements of thermal conductivity on sedimentary rocks. Geothermal Energy, 7(1), 1-36.

[58] Heap, M. J., Kushnir, A. R., Vasseur, J., Wadsworth, F. B., Harlé, P., Baud, P., ... & Deegan, F. M. (2020). The thermal properties of porous andesite. *Journal of Volcanology and Geothermal Research*, 398, DOI: 10.1016/j.jvolgeores.2020.106901.

[59] Heap, M. J., & Kennedy, B. M. (2016). Exploring the scale-dependent permeability of fractured andesite. *Earth and Planetary Science Letters*, *447*, 139-150.

[60] Farquharson, J. I., Heap, M. J., Lavallée, Y., Varley, N. R., & Baud, P. (2016). Evidence for the development of permeability anisotropy in lava domes and volcanic conduits. *Journal of Volcanology and Geothermal Research*, *323*, 163-185.

[61] Brace, W., Walsh, J. B., & Frangos, W. T. (1968). Permeability of granite under high pressure. *Journal of Geophysical Research*, *73*(6), 2225-2236.

[62] Forchheimer, P. (1901). Wasserbewegung durch boden. *Z. Ver. Deutsch, Ing.*, *45*, 1782-1788.

[63] Klinkenberg, L. J. (1941). The permeability of porous media to liquids and gases. In Drilling and production practice. American Petroleum Institute.

[64] Heap, M. J., Kushnir, A. R., Gilg, H. A., Wadsworth, F. B., Reuschlé, T., & Baud, P. (2017). Microstructural and petrophysical properties of the Permo-Triassic sandstones (Buntsandstein) from the Soultz-sous-Forêts geothermal site (France). *Geothermal Energy*, *5*(1), 26.

[65] Lockner, D. (1993). The role of acoustic emission in the study of rock fracture. In *International Journal of Rock Mechanics and Mining Sciences & Geomechanics Abstracts*, 30, No. 7, 883-899.

[66] Griffiths, L., Lengliné, O., Heap, M. J., Baud, P., & Schmittbuhl, J. (2018). Thermal cracking in Westerly Granite monitored using direct wave velocity, coda wave interferometry, and acoustic emissions. *Journal of Geophysical Research: Solid Earth*, *123*(3), 2246-2261.

[67] Gottlieb, P., Wilkie, G., Sutherland, D., Ho-Tun, E., Suthers, S., Perera, K., ... & Rayner, J. (2000). Using quantitative electron microscopy for process mineralogy applications. *Jom*, *52*(4), 24-25.

[68] Worden, R. H., Utley, J. E., Butcher, A. R., Griffiths, J., Wooldridge, L. J., & Lawan, A. Y. (2018). Improved imaging and analysis of chlorite in reservoirs and modern day analogues: new insights for reservoir quality and provenance. *Geological Society, London, Special Publications*, *484*, SP484-10.

[69] Pirrie, D., Butcher, A. R., Power, M. R., Gottlieb, P., & Miller, G. L. (2004). Rapid quantitative mineral and phase analysis using automated scanning electron microscopy (QemSCAN); potential applications in forensic geoscience. *Geological Society, London, Special Publications*, *232*(1), 123-136.

[70] Ayling, B., Rose, P., Petty, S., Zemach, E., & Drakos, P. (2012). QEMSCAN (Quantitative evaluation of minerals by scanning electron microscopy): capability and application to fracture characterization in geothermal systems. In *Proc, Thirty-Seventh Workshop on Geotherm Reserv Eng. Stanford, California: Stanford University*.

[71] Wallace, P. A., De Angelis, S. H., Hornby, A. J., Kendrick, J. E., Clesham, S., von Aulock, F. W., ... & Lavallée, Y. (2019). Frictional melt homogenisation during fault slip: Geochemical, textural and rheological fingerprints. *Geochimica et Cosmochimica Acta*, *255*, 265-288.

[72] Kearsley, E. P., & Wainwright, P. J. (2002). The effect of porosity on the strength of foamed concrete. *Cement and concrete research*, *32*(2), 233-239.

[73] Lian, C., Zhuge, Y., & Beecham, S. (2011). The relationship between porosity and strength for porous concrete. *Construction and Building Materials*, *25*(11), 4294-4298.

[74] Chen, X., Wu, S., & Zhou, J. (2013). Influence of porosity on compressive and tensile strength of cement mortar. *Construction and Building Materials*, *40*, 869-874.

[75] Kumar, R., & Bhattacharjee, B. (2004). Assessment of permeation quality of concrete through mercury intrusion porosimetry. *Cement and Concrete Research*, *34*(2), 321-328.

[76] Nambiar, E. K., & Ramamurthy, K. (2007). Sorption characteristics of foam concrete. *Cement and Concrete Research*, *37*(9), 1341-1347.

[77] McIntosh, R. M., Sharp, J. H., & Wilburn, F. W. (1990). The thermal decomposition of dolomite. *Thermochimica Acta*, *165*(2), 281-296.

[78] Maitra, S., Choudhury, A., Das, H. S., & Pramanik, M. J. (2005). Effect of compaction on the kinetics of thermal decomposition of dolomite under non-isothermal condition. *Journal of Materials Science*, *40*(18), 4749-4751.

[79] Heap, M. J., Mollo, S., Vinciguerra, S., Lavallée, Y., Hess, K. U., Dingwell, D. B., ... & Iezzi, G. (2013). Thermal weakening of the carbonate basement under Mt. Etna volcano (Italy): implications for volcano instability. *Journal of Volcanology and Geothermal Research*, *250*, 42-60.

[80] Trník, A., Scheinherrová, L., Medveď, I., & Černý, R. (2015). Simultaneous DSC and TG analysis of high-performance concrete containing natural zeolite as a supplementary cementitious material. *Journal of Thermal Analysis and Calorimetry*, *121*(1), 67-73.

[81] Galan, I., Glasser, F. P., & Andrade, C. (2013). Calcium carbonate decomposition. *Journal of Thermal Analysis and Calorimetry*, *111*(2), 1197-1202.

[82] Ozawa, M., Uchida, S., Kamada, T., & Morimoto, H. (2012). Study of mechanisms of explosive spalling in high-strength concrete at high temperatures using acoustic emission. *Construction and Building Materials*, *37*, 621-628.

[83] Heap, M. J., Lavallée, Y., Laumann, A., Hess, K. U., Meredith, P. G., & Dingwell, D. B. (2012). How tough is tuff in the event of fire? *Geology*, *40*(4), 311-314.

[84] Heap, M., Kushnir, A., Griffiths, L., Wadsworth, F., Marmoni, G. M., Fiorucci, M., ... & Reuschlé, T. (2018). Fire resistance of the Mt. Epomeo Green Tuff, a widely-used building stone on Ischia Island (Italy).
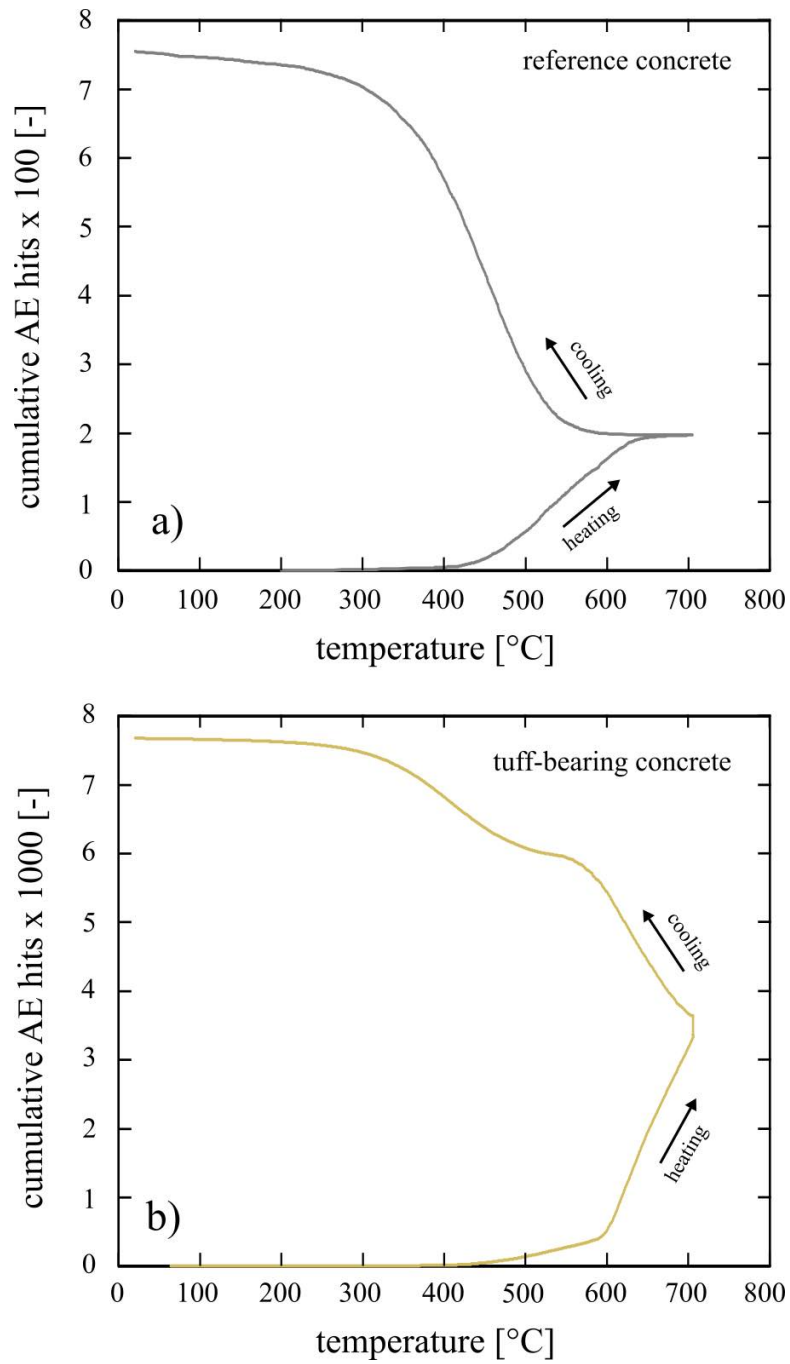
Figures
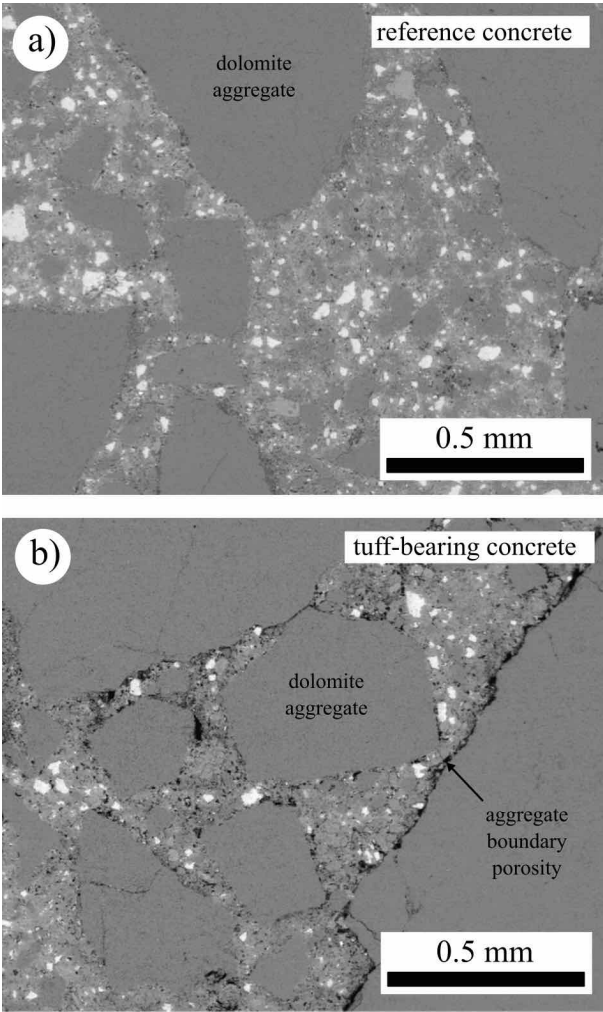
Figure 1. Backscattered scanning electron microscope images of (a) the as-prepared reference concrete and (b) the tuff-bearing concrete (b). See Table 1 for mix ingredients and proportions.
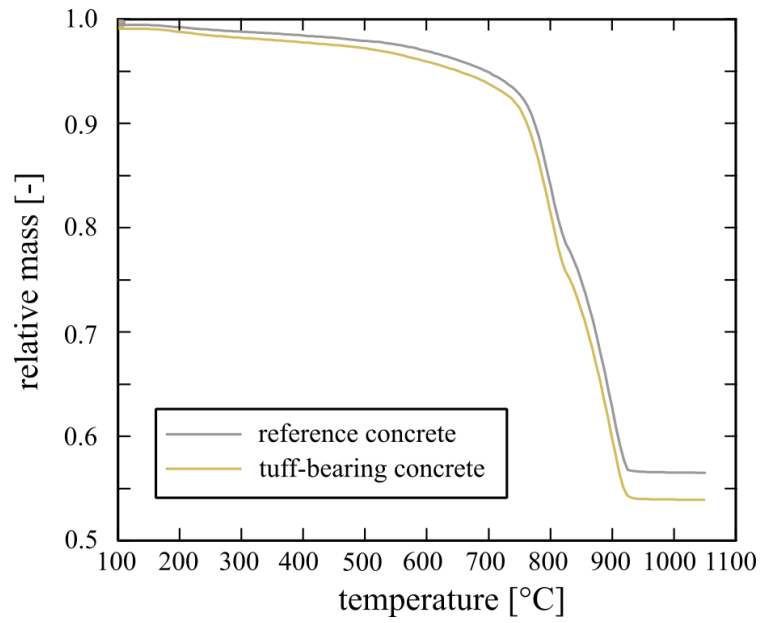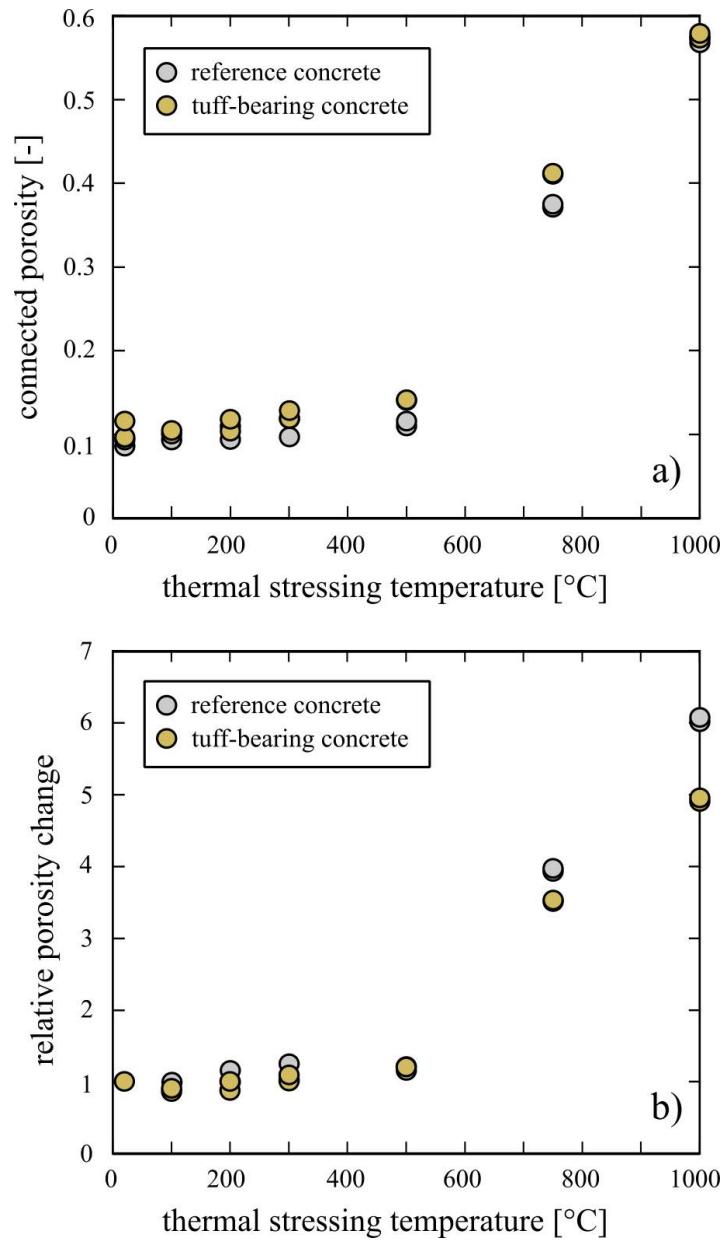
Figure 2. Relative mass of the reference concrete (grey curve) and the tuff-bearing concrete (yellow curve) as a function of temperature (up to 1050 °C). Sample (powders) masses were 69.2 and 74.4 mg for the reference and tuff-bearing concrete, respectively. Samples were heated at a rate of 25 °C/min (see methods section for details).

Figure 3. The number of detected acoustic emission hits during the heating and cooling (at 1 °C/min) of (a) the reference concrete and (b) the tuff-bearing concrete.
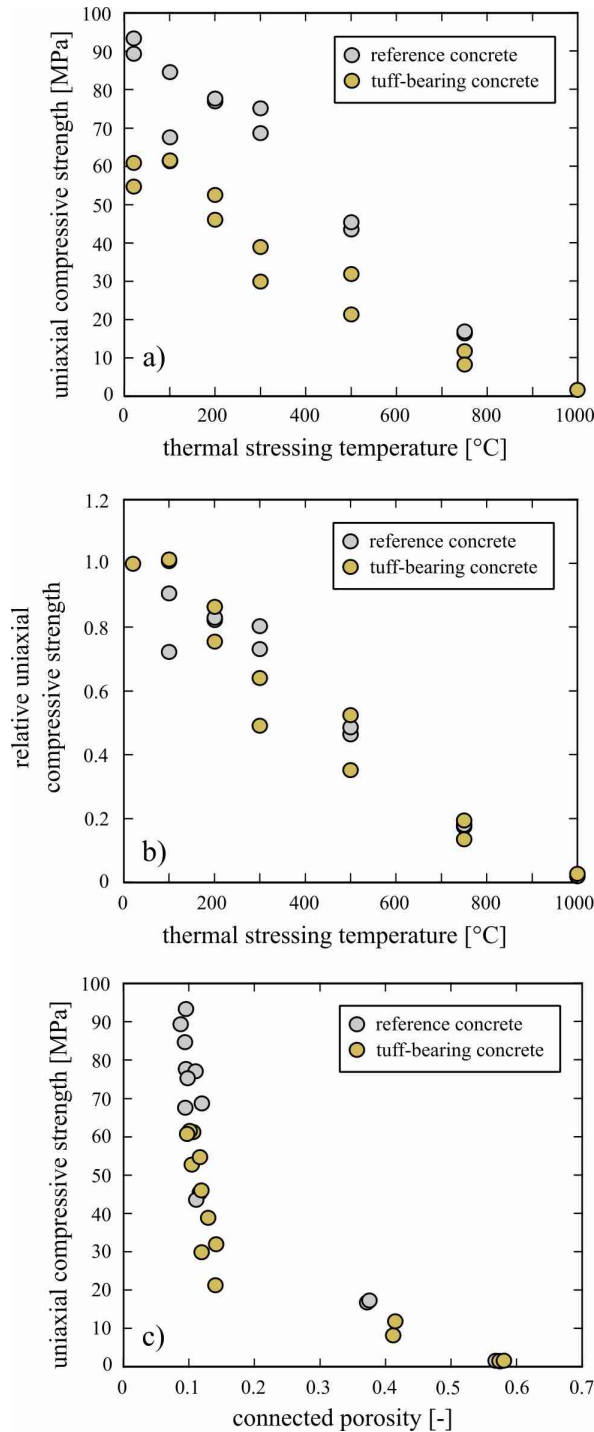
Figure 4. (a) Connected porosity as a function of thermal stressing temperature for the reference concrete (grey circles) and the tuff-bearing concrete (yellow circles). (b) Relative porosity change (as a fraction) as a function of thermal stressing temperature for the reference concrete (grey circles) and the tuff-bearing concrete (yellow circles).
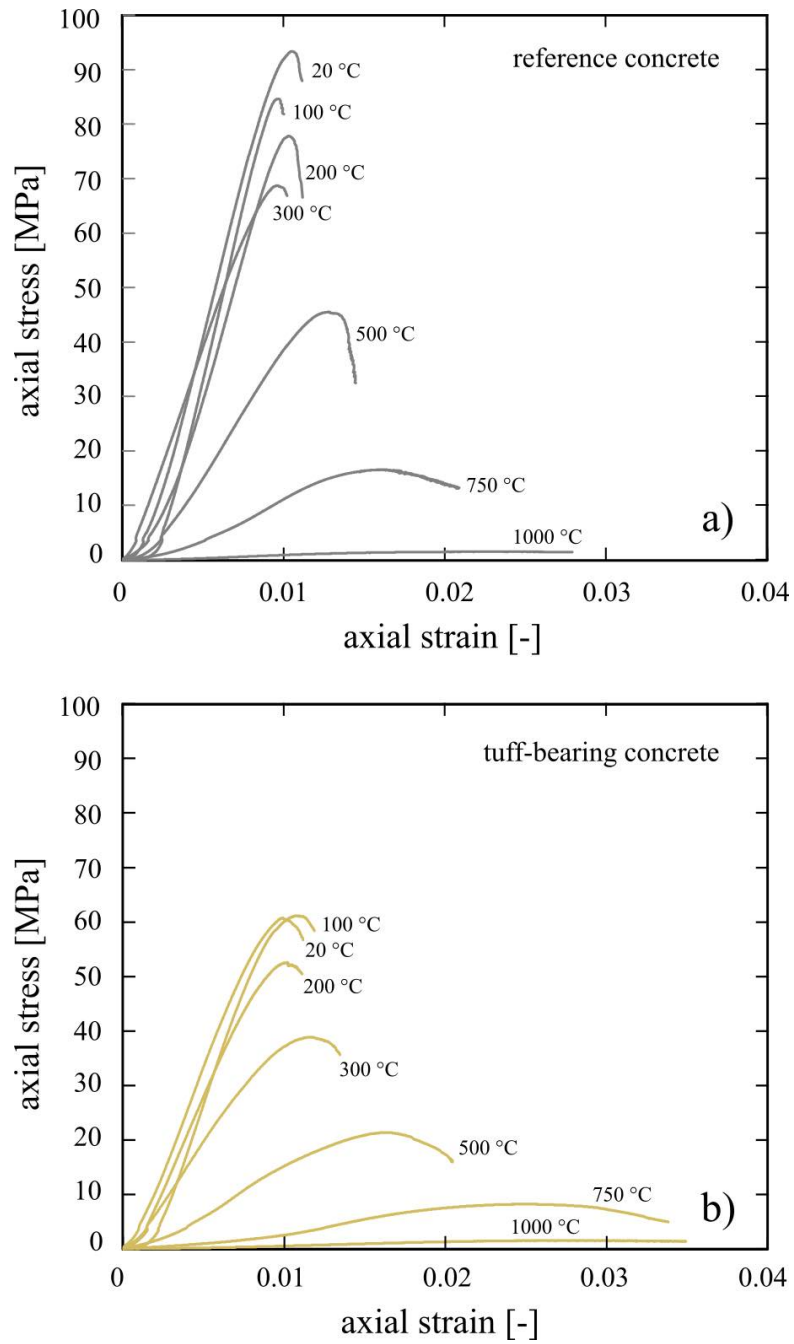
Figure 5. Representative uniaxial stress-strain curves for as-prepared and thermally stressed samples of (a) the reference concrete and (b) the tuff-bearing concrete. The temperature next to each curve indicates the thermal stressing temperature.

Figure 6. (a) Residual uniaxial compressive strength as a function of thermal stressing temperature for the reference concrete (grey circles) and the tuff-bearing concrete (yellow circles). (b) Relative residual uniaxial compressive strength (as a fraction) as a function of thermal stressing temperature for the reference concrete (grey circles) and the tuff-bearing concrete (yellow circles). (c) Residual uniaxial compressive strength as a function of connected porosity for the reference concrete (grey circles) and the tuff-bearing concrete (yellow circles).
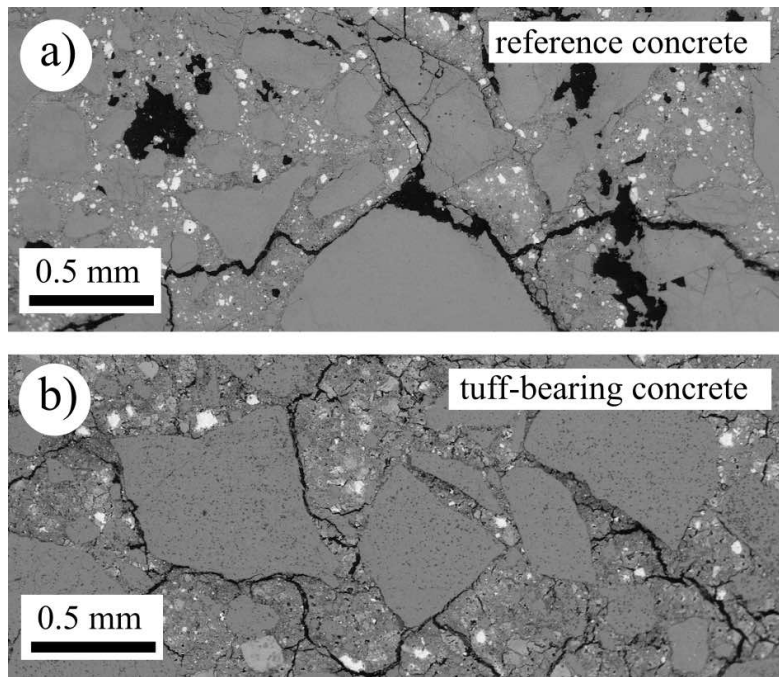
Figure 7. Backscattered scanning electron microscope images showing microcracks within the (a) reference concrete and (b) the tuff-bearing concrete following exposure to 750 °C.
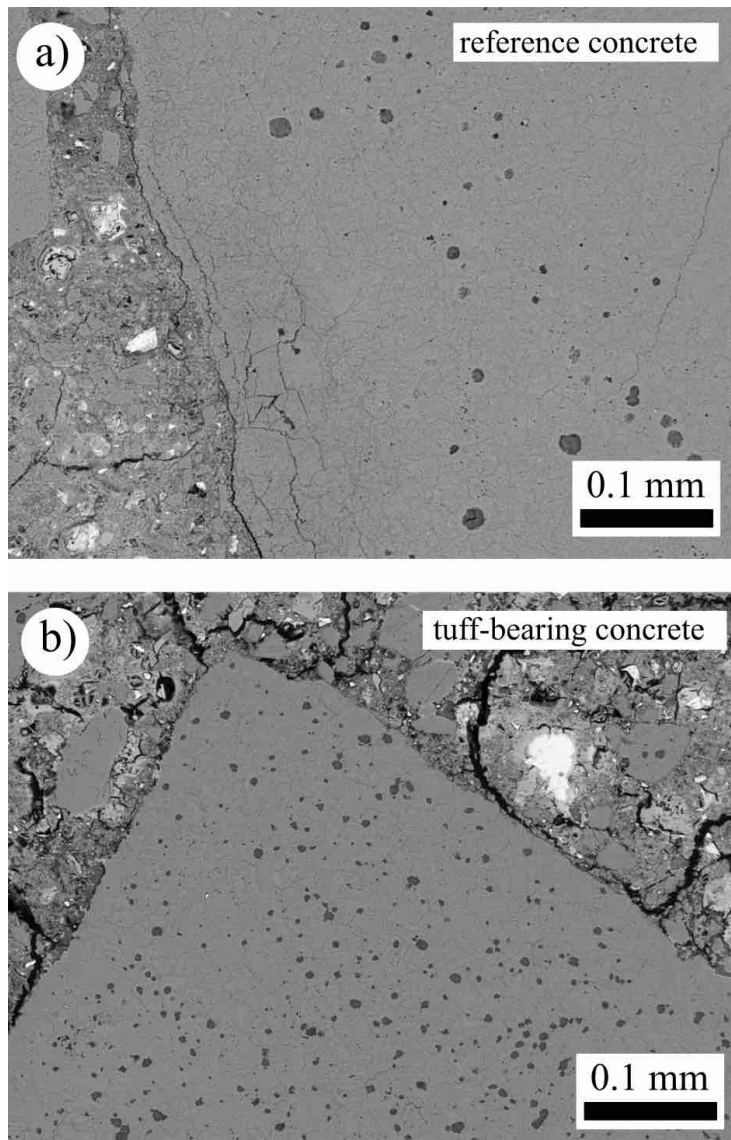
Figure 8. Backscattered scanning electron microscope images showing microcracks and sub-circular pores within the aggregates of (a) the reference concrete and (b) the tuff-bearing concrete following exposure to 750 °C.
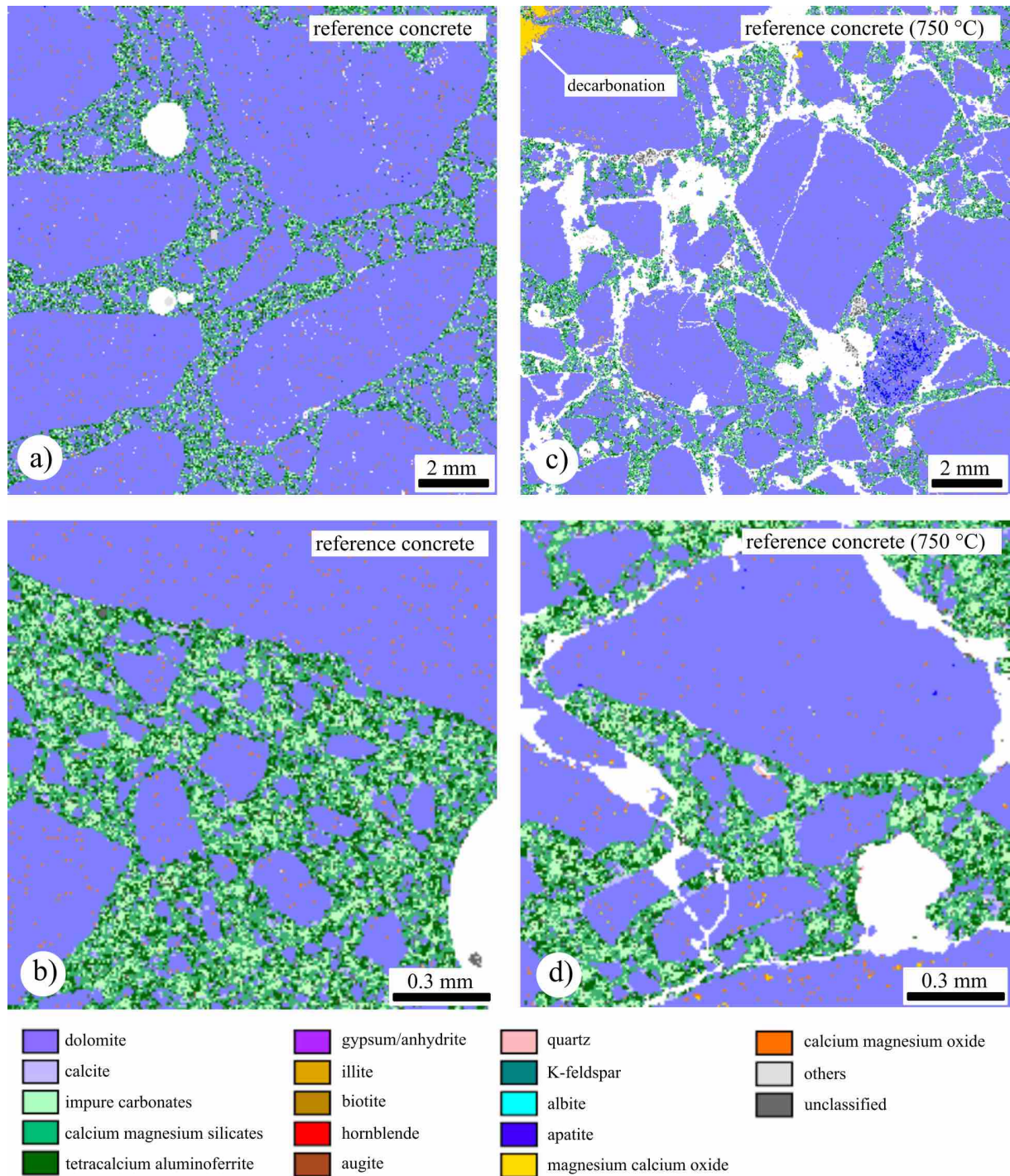
Figure 9. QEMSCAN^TM (Quantitative Evaluation of Minerals by Scanning Electron Microscopy) mineral composition maps for the as-prepared reference concrete at (a) a step size of 20 μm and (b) a step size of 2 μm, and the reference concrete following exposure to 750 °C at (c) a step size of 20 μm, and (d) a step size of 2 μm.
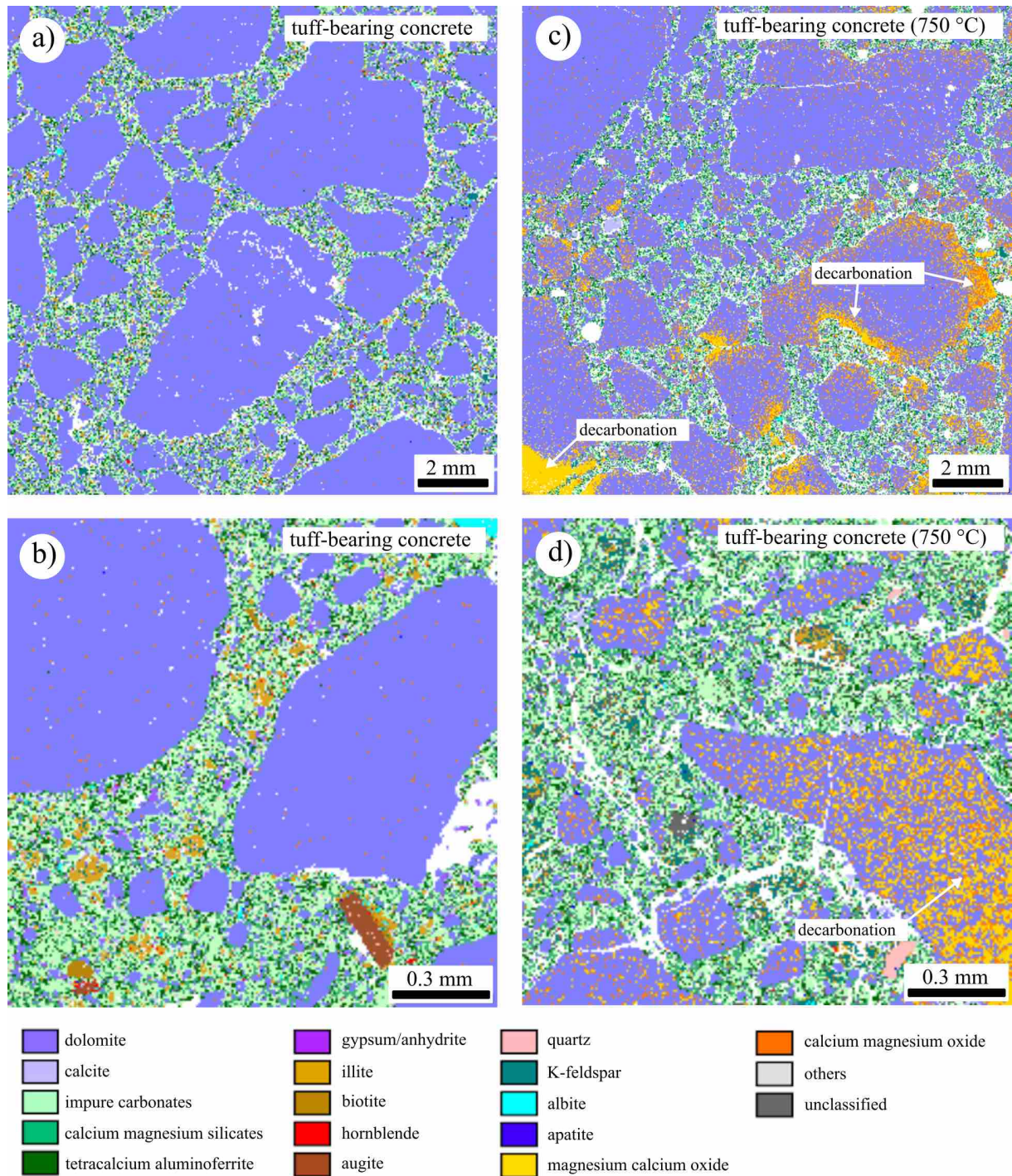
Figure 10. QEMSCAN™ (Quantitative Evaluation of Minerals by Scanning Electron Microscopy) mineral composition maps for the as-prepared tuff-bearing concrete at (a) a step size of 20 μm and (b) a step size of 2 μm, and the tuff-bearing concrete following exposure to 750 °C at (c) a step size of 20 μm, and (d) a step size of 2 μm.
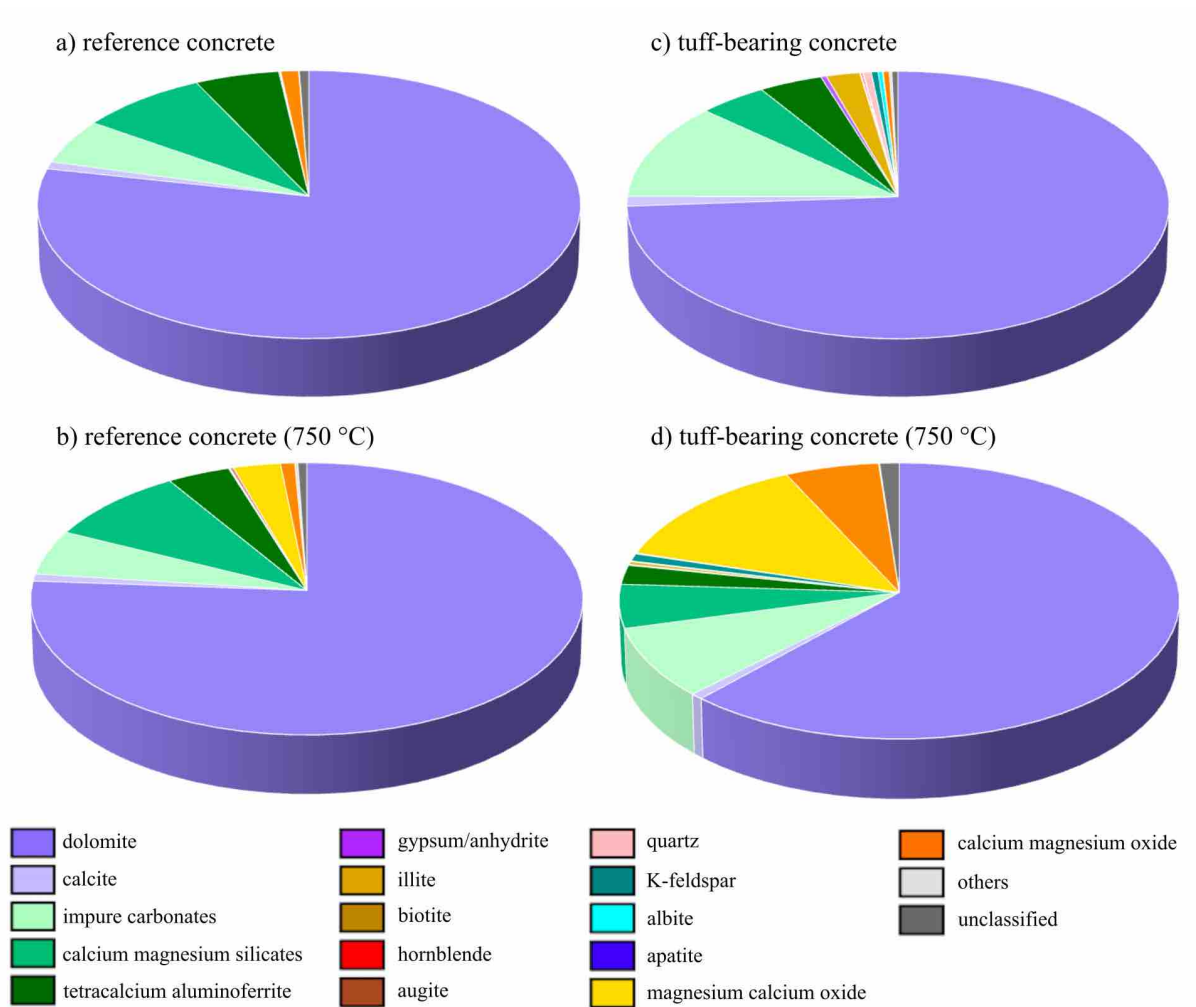
Figure 11. Pie charts showing the mineral composition (as quantified by the QEMSCAN[TM]) of (a) the as-prepared reference concrete, (b) the reference concrete following exposure to 750 °C, (c) the as-prepared tuff-bearing concrete, and (d) the tuff-bearing concrete following exposure to 750 °C (the data are also available in Table 4).

Table 1. Ingredients, and their proportions, used in the preparation of the two types of concrete prepared for this study: a reference concrete (without zeolite-bearing tuff) and a tuff-bearing concrete. See Table 2 for the mineral composition of the zeolite-bearing tuff. If the tuff powder is considered as a binder, the water/binder ratio of the reference and tuff-bearing concretes are 0.69 and 0.53, respectively.

Ingredient	Reference concrete (kg.m^{-3})	Tuff-bearing concrete (kg.m^{-3})
Cement Cem I 52.5 R	320	320
Sand (ϕ 0.5; 1.4 mm)	1045	1045
Gravel (ϕ 4.10; 17 mm)	900	900
Fine aggregate	100	0
Tuff powder (see Table 2)	0	100
Additive Viscocrete 3075	3.2	3.2
Water	220	220

Table 2. Quantitative mineral composition, by X-ray diffraction (CuKα radiation, 40 kV, 30 mA) using an X'Pert instrument (PANalytical), of the zeolite-bearing tuff (from the Campanian Ignimbrite, Italy) used in the preparation of the tuff-bearing concrete (see Table 1). Data taken from de Gennaro et al. [53]. Our QEMSCAN^{TM} analysis also indicates the presence of hornblende and illite (Table 4).

Mineral	Wt.%
Phillipsite	40 ± 1
Chabazite	5 ± 1
Feldspar	24 ± 3
Smectite	4 ± 1
Quartz	5 ± 1
Calcite	4 ± 1
Analcime	6 ± 1
Biotite	Trace
TOTAL	88

Table 3. Bulk sample density, connected porosity, and residual uniaxial compressive strength of the reference and tuff-bearing concretes exposed to different temperatures (see Table 1 for mix ingredients and proportions). "R" – Reference; "T" – tuff-bearing.

Concrete	Temperature (°C)	Bulk sample density (kg/m³)	Connected porosity	Uniaxial compressive strength (MPa)
R	20	2540	0.087	89.5
R	20	2506	0.094	93.4
R	100	2495	0.094	67.6
R	100	2489	0.094	84.7
R	200	2481	0.110	77.0
R	200	2540	0.094	77.9
R	300	2461	0.119	68.8
R	300	2518	0.098	75.2
R	500	2486	0.110	43.6
R	500	2479	0.116	45.6
R	750	1843	0.375	17.4
R	750	1855	0.371	16.7
R	1000	1450	0.568	1.6
R	1000	1424	0.575	1.5
T	20	2449	0.117	54.7
T	20	2516	0.097	60.8
T	100	2406	0.101	61.8
T	100	2401	0.106	61.2
T	200	2518	0.104	52.6
T	200	2473	0.119	45.9
T	300	2476	0.119	29.9
T	300	2441	0.129	38.9
T	500	2397	0.142	31.9
T	500	2354	0.141	21.4
T	750	1736	0.414	11.8
T	750	1748	0.411	8.3
T	1000	1402	0.580	1.6
T	1000	1422	0.574	1.6

Table 4. Mineral composition, and their proportions, measured using the QEMSCAN™ (see text for details) on thin sections of (1) the as-prepared reference and tuff-bearing concretes and (2) the reference and tuff-bearing concretes following exposure to 750 °C.

Mineral	As-prepared reference concrete (%)	Reference concrete after 750 °C (%)	As-prepared tuff-bearing concrete (%)	Tuff-bearing concrete after 750 °C (%)
Dolomite	78.35	76.12	73.88	61.82
Calcite	0.89	0.85	1.17	0.68
Impure carbonates	5.40	5.31	11.69	8.34
Calcium magnesium silicates	8.15	8.95	4.37	5.12
Tetracalcium aluminoferrite	5.32	3.93	4.02	2.25
Gypsum/anhydrite	0.08	0.00	0.36	0.12
Illite	0.00	0.00	2.12	0.31
Biotite	0.00	0.00	0.06	0.03
Hornblende	0.00	0.00	0.11	0.01
Augite	0.00	0.01	0.04	0.02
Quartz	0.02	0.08	0.51	0.05
K-feldspar	0.00	0.00	0.43	0.87
Albite	0.00	0.00	0.28	0.09
Apatite	0.02	0.21	0.03	0.03
Magnesium calcium oxide	0.00	2.93	0.00	13.27
Calcium magnesium oxide	1.13	0.89	0.40	5.75
Others	0.03	0.18	0.15	0.05
Unclassified	0.61	0.56	0.39	1.20
TOTAL	100.00	100.01	100.01	100.01